



Two-dimensional numerical investigation on the dynamics of ligament formation by Faraday instability



Yikai Li*, Akira Umemura

Department of Aerospace Engineering, Nagoya University, Furo-cho, Chikusa-ku, Nagoya 464-8603, Japan

ARTICLE INFO

Article history:

Received 14 June 2013

Received in revised form 3 November 2013

Accepted 3 December 2013

Available online 12 December 2013

Keywords:

CLSVOF

Faraday instability

Ligament

Nonlinear effect

ABSTRACT

Ligament formation from the surface of a horizontal liquid layer subject to a vertical vibration (Faraday instability) is a crucial part of the atomization process because it is the transition phase for droplet generation. Based on the numerical solutions of the two-dimensional incompressible Euler equations for a prototype Faraday instability flow, we explored physically how a liquid ligament that is dynamically free from the vibrating liquid layer and behaves like a jet can be produced. According to linear theory, the suction of liquid from the trough portion to the crest portion creates an amplified crest. The amplified crest is always pulled back to the liquid layer in linear theory, no matter how largely the surface deforms; thus, a dynamically freed ligament never forms. However, under nonlinear conditions produced by large surface deformation, the impinging liquid flow from the trough portion enhances the pressure at the high crest (ligament) root. This pressure enhancement has two major effects. First, it reduces the amount of liquid sucked from the trough portion, which abates the increase in the crest height compared with that associated with linear theory. Second, it forms a local maximum pressure at the crest root; in this case, the ligament above this location becomes dynamically free from the motion of the bottom substrate in the laboratory reference frame. Liquid elements continuously enter the dynamically freed liquid region, producing a slender ligament from the liquid layer.

© 2013 Elsevier Ltd. All rights reserved.

1. Introduction

Liquid atomization plays an important role in a wide range of industrial applications. For example, in an automotive engine, especially a diesel engine, the combustion efficiency and emission quality are highly dependent on the fuel spray and atomization characteristics. Other fields where liquid atomization is applied include pharmaceutical emulsification, encapsulation, and ink-jet printing. The increasing importance of liquid atomization in various industrial processes requires a better understanding of the underlying physical dynamics to further enhance the process.

Many techniques have been used to realize liquid atomization. One practical method is subjecting a body of liquid to a vertical vibration to produce droplets from its surface. When the forcing acceleration amplitude is small, standing waves are often observed on the surface. This phenomenon was first studied by Faraday (1831); thus, it is referred to as a “Faraday instability” and the resultant surface standing waves are called “Faraday waves”. A theoretical analysis of a Faraday instability in the linear regime was carried out by Benjamin and Ursell (1954) for ideal fluids. They obtained an instability chart based on two parameters X and Y

(defined by Eq. (2)), which are related to the forcing displacement amplitude and the frequency. Faraday waves and associated nonlinear effects were reviewed by Miles and Henderson (1990). Kumar (1996) and Kumar and Tuckerman (1994) studied the effects of viscosity on atomization using linear stability analysis. When the forcing acceleration amplitude is enhanced sufficiently beyond Faraday wave formation, ligaments (or spikes) disintegrating into droplets are created from the liquid surface. One typical application of such a technique is the so-called “ultrasonic atomization”, the forcing frequency of which is on the order of 10 kHz to 1 MHz. This phenomenon was first investigated by Wood and Loomis (1927). Experimental research was then conducted by Lang (1962), who derived a correlation between the median droplet diameter and the forcing frequency in the frequency range of 10–800 kHz. Rajan and Pandit (2001) studied the effects of the liquid properties including the flow rate, viscosity, density, and surface tension, and the ultrasonic properties including the forcing displacement amplitude and frequency to predict the droplet size. Al-Sueimani et al. (1999), Yule and Al-Suleimani (2000), Al-Suleimani and Yule (2002) investigated the disorder in surface standing waves using high-speed imaging techniques to explain the random ejection locations and the range of droplet sizes generated by ultrasonic atomization. Goodridge et al. (1996, 1997, 1999) studied the threshold conditions for droplet ejection

* Corresponding author. Tel.: +81 52 789 4405.

E-mail address: li.yikai@f.mbox.nagoya-u.ac.jp (Y. Li).

by a Faraday instability at low frequencies below 100 Hz. The threshold forcing acceleration amplitude is dependent on the surface tension and forcing frequency for low-viscosity liquids, and on the viscosity and forcing frequency for high-viscosity liquids.

Besides atomizing the liquid layer by vertical vibration (Faraday instability), similar atomization techniques that exploit the vibration have been proposed recently. Tsai et al. (1996, 1997) invented a new spray technique known as “ultrasound-modulated two-fluid (UMTF) atomization”, which utilizes the resonance between the liquid capillary waves generated by ultrasound and those generated by air to create a relatively narrow droplet-size distribution. James et al. (2003a,b) and Vukasinovic et al. (2004, 2007) introduced a method known as “vibration-induced drop-atomization (VIDA)” to atomize a parent liquid drop resting on a vibrating horizontal diaphragm into a spray. Moreover, Qi et al. (2008) and Tan et al. (2010) numerically and experimentally studied surface acoustic wave (SAW) atomization, which rapidly generates micron-size aerosol droplets.

The nonlinear nature of the atomization phenomenon introduces great complexity into its mathematical treatment. Moreover, due to its inherently small temporal and spatial scales, it is difficult to determine the underlying atomization mechanism solely by experiments. Recent improvements to computer capacity and numerical schemes allow information to be extracted from detailed flow-field data, which are difficult to measure experimentally. As a result, increasingly more numerical investigations have been conducted to study the fundamental physics of atomization (Al-Sueimani et al., 1999; Wright et al., 2000; Al-Sueimani and Yule, 2002; James et al., 2003b; Shinjo and Umemura, 2010; Takagi and Matsumoto, 2011).

Any atomization process can, in general, be divided into two sub-processes: ligament (or spike) formation from the liquid surface, and disintegration of the ligament into droplets. The mechanism of the latter process, studied extensively through liquid column disintegration research (Eggers, 1997; Eggers and Villermaux, 2008; Umemura, 2011), does not crucially depend on the way the ligament is formed. The disintegration of the ligament into droplets is not the focus of this study.

For a liquid jet emitted from a nozzle, ligaments can be formed by the action of gaseous suction pressure/shear stress on the crest of the liquid jet surface (Shinjo and Umemura, 2010). In a Faraday instability, the gaseous effect is not essential; this suggests that some other mechanism must be required for ligament formation.

The major forces determining the dynamics of large surface deformation (ligaments or spikes at the liquid surface) or breakups induced by vibration are the inertial force, viscous force, gravitational force, and capillary force. Yule and Al-Sueimani (2000) experimentally studied the disorderliness of droplet formation. They claimed that the Froude number (inertial force/gravitational force) does not affect the droplet size or droplet formation process. James et al. (2003b) numerically studied the effect of the Reynolds number (inertial force/viscous force), the dimensionless forcing acceleration amplitude (inertial force/capillary force), and the Bond number (gravitational force/capillary force) on the volume and velocity of the ejected drop and the time of ejection in VIDA at low forcing frequencies. Vukasinovic et al. (2004) experimentally studied the mechanism of free surface breakup in VIDA at forcing frequencies on the order of 1 kHz. They established the dependence of the breakup time and the unbroken spike length on the capillary number (viscous force/capillary force). Donnelly et al. (2004) experimentally studied the droplet diameter distribution at frequencies on the order of 1 MHz. They determined that the relationship between the droplet size and forcing frequency follows an inviscid scaling law. Qi et al. (2008) experimentally and numerically studied SAWs; they determined that the growth of the interfacial wave was caused by a destabilizing effect due

to the large acoustic irradiation overwhelming the stabilizing and restoring effect of the capillary force.

However, these previous studies have focused mainly on the dynamics or mechanisms of droplet formation. Studies of the detailed dynamics of ligament formation from a liquid layer by a Faraday instability, especially numerical attempts, have been limited. Thus far, it has been established that the inertial effect plays an essential role in ligament formation. To quantify the condition for spray formation by a Faraday instability, we must reveal the physical mechanism of how the inertial effects produce large surface deformation that is dynamically free from the motion of the bottom substrate by fully analyzing the detailed velocity and pressure fields. The term “ligament” in this study is thus specifically defined as a large liquid surface deformation that is dynamically free from the vibrating bottom substrate and results in disintegrated droplets having outward velocities (i.e., the condition for spray formation). To our knowledge, there is no literature addressing this mechanism in detail. Therefore, we conducted the present numerical research.

The rest of this paper is organized as follows. The physical model and the numerical setup are described in Section 2. Test calculations are conducted to validate the numerical code in both the linear and nonlinear regimes in Section 3. The dynamics of the ligament formation are analyzed in detail based on a prototype in Section 4. Finally, the results of this study are summarized in Section 5.

2. Problem specification and numerical method

2.1. Physical model used for calculation

We consider a liquid layer resting horizontally on a substrate, subject to a vertical vibration of standard sinusoidal displacement, $\Delta_0 \sin(\Omega t)$, where Δ_0 is the amplitude of the forcing displacement, Ω is the forcing frequency, and t is the time. Before proposing a physical model for the calculation, we concisely review the inviscid linear theory derived by Benjamin and Ursell (1954) to introduce the system parameters described in the introduction.

Any surface deformation can be expressed by a Fourier series in the horizontal coordinate x . Each Fourier component $a = \delta(t) \sin(kx)$ (where k is the wavenumber) is independent of the others in the linear regime. The amplitude $\delta(t)$ obeys the Mathieu equation

$$\frac{d^2 \delta}{dt^2} = (X \sin \hat{t} - Y) \cdot \delta, \quad (1)$$

where $\hat{t} = \Omega t$. The linear stability of the liquid layer is determined by two parameters X and Y , defined as

$$X = k \Delta_0 \tanh(ky_0) \quad \text{and} \quad Y = \left(\frac{\omega}{\Omega}\right)^2 = \frac{\sigma k^3 \tanh(ky_0)}{\rho_l \Omega^2}, \quad (2)$$

where y_0 is the thickness of the liquid layer, σ is the surface tension coefficient, and ρ_l is the liquid density. For each parameter pair (X , Y), we obtain a solution of the surface deformation amplitude $\delta(t)$, from the behavior of which we can determine whether or not the motion of the free surface is stable and the response of the surface oscillation is sub-harmonic, harmonic, or higher-order harmonic. The instability conditions derived from linear theory are charted in Fig. 1 as hatched regions.

An experiment with certain values of the forcing displacement amplitude and frequency (Δ_0 , Ω) can be described by a cubic curve, as shown in Fig. 1, by eliminating k from Eq. (2). Under the assumption $\tanh(ky_0) \rightarrow 1$, the curve is expressed as

$$Y = X^3 \left(\frac{\sigma}{\rho_l \Delta_0^3 \Omega^2} \right) = \frac{X^3}{\beta}, \quad (3)$$

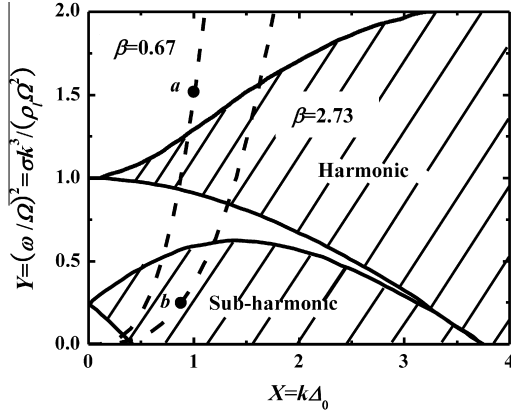


Fig. 1. Instability regions (hatched regions) for the Mathieu equation. Whether the surface waves are stable or not depends on the parameter pair (X, Y) . In the harmonic regime, the resulting surface wave frequency is equal to the forcing frequency Ω , while in the sub-harmonic regime, the resulting surface wave frequency is equal to one half the forcing frequency Ω . Each dashed curve $Y = X^3/\beta$ corresponds to certain dimensionless forcing acceleration amplitude $\beta = \rho_1 \Delta_0^2 \Omega^2 / \sigma$. The two symbols labeled as “a” and “b” correspond to the parameter pairs $(X = 1, Y = 1.5)$ and $(X = 0.88, Y = 0.25)$, respectively, which are the cases used for numerical calculations conducted in Section 3.

where $\beta = \rho_1 \Delta_0^2 \Omega^2 / \sigma$ is the dimensionless forcing acceleration amplitude. All of the unstable wavenumbers that can lead to ligament formation under this dimensionless forcing acceleration amplitude should be located on this curve in the instability regions. Ultrasonic atomization experiments have shown that the mean diameter of the atomized droplets is related to the frequency according to $d_m \cong 0.34\lambda \sim c(1/\Omega)^{2/3}$ (Lang, 1962; Donnelly et al., 2004), where c is a constant when liquid properties are specified. This indicates the existence of one predominant wavelength, $\lambda = 2\pi/k$, for a surface deformation for each forcing acceleration amplitude. Therefore, we conducted a typical single wavenumber calculation for certain forcing acceleration amplitudes as a prototype to illustrate the basic dynamics. The thickness of the full liquid layer in the ultrasonic atomization experiments ($\sim \text{cm}$) is far larger than the predominant surface wavelength ($\sim \mu\text{m}$). As demonstrated later, the main dynamics associated with ligament formation are limited to a depth of $1/k$ from the surface; liquid located deeper than $1/k$ essentially moves with the vibrating plate. Thus, simulating the full liquid layer is unnecessary for our purpose. In this study, we only considered the cases where the liquid layer thickness was $y_0 = \lambda$ and $y_0 = \lambda/4$, which are both larger than the effective dynamic depth $1/k$. The appropriate calculation domain to be used is illustrated in Fig. 2 for a two-dimensional (2-D) configuration.

In this study, as the first step in a three-dimensional (3-D) problem, which requires extremely large calculation times, we first considered a 2-D problem. Wright et al. (2000) and Takagi and Matsumoto (2011) showed that 2-D calculation captures the characteristic nonlinear dynamics of a Faraday instability, i.e., large surface deformation from the liquid layer. However, the detailed flow structures and the dynamics of ligament formation, in which we are interested in the present paper, were not analyzed in their research.

Additional assumptions were made for simplicity, which are given as follows. The effects of viscosity and gravity were ignored in this study. The viscous damping effect suppresses the breakup (Goodridge et al., 1997; James et al., 2003b; Vukasinovic et al., 2004). However, for the forcing frequency range $f/f_* < 0.1756$, where $f = \Omega/(2\pi)$, $f_* = (\sigma/\rho_1)^{1/2}/v_1^3$, and v_1 is the liquid kinetic viscosity, the vibrating liquid can be considered to be in the inviscid regime (Donnelly et al., 2004). For example, the inviscid assumption is valid when the frequency is less than $f_u = 0.1756$

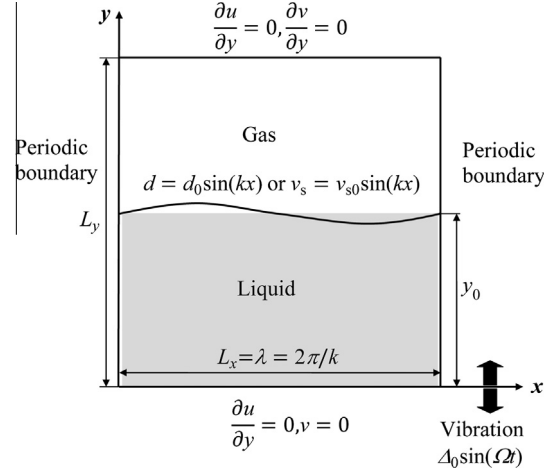


Fig. 2. Schematic illustration of the calculation domain, boundary conditions and initial condition.

$f_* \sim 100$ MHz for distilled water, which is even larger than the frequency usually used in practice for ultrasonic atomization experiments (~ 1 MHz). Furthermore, capillary effects dominate over gravitational effects when $f > f_b = g^{3/4}(\rho_1/\sigma)^{1/4}/(2\pi)$ (Donnelly et al., 2004), where g is the acceleration due to gravity. As a result, it is reasonable to neglect gravity when the forcing frequency is larger than $f_b = 10$ Hz for distilled water. The frequencies f_u and f_b provide the upper and lower limits of this study.

In the frame of reference moving with the vibrating substrate, the imposed acceleration is mediated by an oscillatory body force (the inertial force). The governing equations to be solved for both the liquid and gas phases are

$$\nabla \cdot \mathbf{u} = 0$$

$$\rho \left[\frac{\partial \mathbf{u}}{\partial t} + (\mathbf{u} \cdot \nabla) \mathbf{u} \right] = -\nabla p + \rho \Delta_0 \Omega^2 \sin(\Omega t) \mathbf{e}_y + \mathbf{F}_s, \quad (4)$$

where \mathbf{u} is the velocity vector, whose vertical component is the one referring to the substrate, ρ is the density defined by Eq. (7), p is the pressure, \mathbf{e}_y is the unit vertical vector, and \mathbf{F}_s is the body force vector expressing the surface tension force in the continuum surface force (CSF) model (Brackbill et al., 1992) described later.

The calculation domain and boundary conditions are specified in Fig. 2. In the moving frame of reference, the bottom boundary was treated as a slip condition. Because only one wavelength span ($L_x = \lambda = 2\pi/k$) was considered, periodic conditions were imposed on the left and right sides of the rectangular calculation domain. The top gas edge was established as a free boundary. Initially, both the liquid and gas phases were set to be stagnant, except for the interface which was disturbed to initiate the Faraday instability. In this study, the initial disturbance was introduced as the imposition of a vertical surface velocity distribution $v_s = v_{s0} \sin(kx)$, where v_{s0} is a small value compared with the amplitude of the vibration velocity. This definition of disturbance is equivalent to the imposition of an initial surface displacement distribution $d = d_0 \sin(kx)$ and simplifies the numerical conduction in this study. Unless otherwise specified, the flow movement is hereafter described in the frame of reference moving with the vibrating substrate.

2.2. Numerical method

The governing equations were discretized on a uniform, staggered grid. The velocity vector was stored at the cell edge, while the pressure and density were stored at the cell center. This grid configuration is suitable for the “marker-and-cell (MAC)” method

(Harlow and Welch, 1965) used to solve the temporal evolution of the pressure and velocity fields. Sixty-four horizontal grid points were assigned to one wavelength.

An explicit second-order upwind scheme for discretization of the convective terms, coupled with the second-order Runge–Kutta method for temporal integration, was used to advance the intermediate velocity. In general, this intermediate velocity does not satisfy the continuum equation due to the pressure change. A Poisson equation for pressure, with the divergence of the intermediate velocity as the source term, was then derived to calculate the pressure change. The solution of this Poisson equation determined the velocity field at the next time step. The discrete Poisson equation was solved by the traditional Gauss–Seidel iteration method, and the convergence criterion was set as a residual of 10^{-10} . The time step was adjusted in each calculation cycle to retain stability. The time step must satisfy the inequality given below (Nichols et al., 1980):

$$\Delta t \leq \min \left[C \frac{\Delta x}{|u_{\max}|}, C \frac{\Delta y}{|v_{\max}|}, \sqrt{\frac{\min(\rho_l, \rho_g)}{4\sigma}} \min(\Delta x, \Delta y)^3 \right], \quad (5)$$

where C , the Courant number, was set to 0.25 in our calculations, with $\Delta x = \Delta y = \lambda/64$.

The body force \mathbf{F}_s evaluated by the CSF method is given by

$$\mathbf{F}_s = \sigma \kappa \nabla H_\varepsilon. \quad (6)$$

The surface tension force was transformed into a volume force and scattered in a region around the interface (having a constant thickness ε in the CSF model); κ is the curvature and H_ε is the smoothed Heaviside function with thickness ε .

The phase interface is usually represented implicitly by introducing two kinds of functions: a level set (LS) function ϕ (the signed normal distance to the interface) or a volume-of-fluid (VOF) function F (the fraction of the concerned fluid (liquid) in each cell). The LS method (Sussman et al., 1994; Sussman and Fatemi, 1999; Sethian and Smereka, 2003) has merits in evaluating curvature due to the continuity nature of ϕ , but it usually loses conservation of volume in the re-initialization step required to keep its distance property. Although Sussman and Fatemi (1999) proposed a constraint in the re-initialization process to improve its performance in volume conservation, the results were still unsatisfactory. The VOF method (Nichols et al., 1980; Hirt and Nichols, 1981; Rider and Kothe, 1998) is inherently a volume-conserving method, but its poor behavior in evaluating curvature due to its step-like properties around interfaces limits its application. The coupled level-set volume-of-fluid (CLSVOF) method (Sussman and Puckett, 2000; Renardy and Renardy, 2002; Sussman, 2003; Van der Pijl et al., 2005; Popinet, 2009), taking advantages of both methods, has attracted significant attention recently with regard to multi-phase calculation. The mass-conserving level-set (MCLS) method (Van der Pijl et al., 2005) was adopted in this study.

We initially set ϕ to be the signed normal distance to the interface (for a liquid, $\phi > 0$; for a gas, $\phi < 0$). $F = 0$ for a cell with pure gas; $F = 1$ for a cell with liquid only. A cell occupied partially by liquid can be calculated from an explicit function $F = F(\phi, \nabla \phi)$ by assuming that the interface in this cell is a straight line. This idea is similar to piecewise linear interface construction (PLIC) (Rider and Kothe, 1998), with the slope of the line segment determined by ϕ . The density in each cell is given by

$$\rho = \rho_l \cdot H_\varepsilon(\phi) + \rho_g \cdot [1 - H_\varepsilon(\phi)], \quad (7)$$

with a density ratio of $\rho_l/\rho_g = 50$ to confirm the calculation stability. The curvature κ can be determined from ϕ according to

$$\kappa = -\nabla \cdot \frac{\nabla \phi}{|\nabla \phi|}. \quad (8)$$

Note that ρ , ϕ , and F are all defined at the cell center. After the velocity field is determined at each new time step, convection of ϕ and F provides the following:

$$\frac{\partial \phi}{\partial t} + (\mathbf{u} \cdot \nabla) \phi = 0, \quad (9)$$

and

$$\frac{\partial F}{\partial t} + (\mathbf{u} \cdot \nabla) F = 0. \quad (10)$$

Eq. (9) was solved by the second-order essential non-oscillation (ENO) scheme (Sussman and Fatemi, 1999), and Eq. (10) was solved by geometrical convection of the reconstructed line segment. Re-initialization was required to revise the level set function ϕ to retain its definition of the signed normal distance function ($|\nabla \phi| = 1$)

$$\frac{\partial \phi}{\partial \tau} = \text{sign}(\phi)(1 - |\nabla \phi|), \quad (11)$$

where τ is a virtual time. Another explicit function, $\phi = G(F, \nabla \phi)$, was used to iteratively approach a new level set function to preserve volume conservation. With this method, the largest volume variation for all calculation cases was less than one percent of the entire liquid volume.

3. Numerical validations

3.1. Linear regime

To investigate the performance of the utilized CLSVOF method, we first used linear regime calculation to compare with linear predictions (Benjamin and Ursell, 1954). When the initial disturbance imposed on the surface is small and the parameter pair (X, Y) is located in a stable region, the amplitude of the surface deformation is retained within a small magnitude (Wright et al., 2000). We considered the case $(X=1, Y=1.5)$ and $y_0 = \lambda$, corresponding to the following real physical conditions: $\rho_l = 1000 \text{ kg m}^{-3}$, $\rho_g = 20 \text{ kg m}^{-3}$, $\sigma = 0.072 \text{ N m}^{-1}$, $\Omega = 6.28 \times 10^6 \text{ rad s}^{-1}$ ($f = 1 \text{ MHz}$), $\lambda = 6.71 \text{ }\mu\text{m}$, $\Delta_0 = 1.07 \text{ }\mu\text{m}$, and $\beta = 0.67$, which is denoted by the label “a” in Fig. 1. Fig. 3 shows the temporal evolution of the calculated surface displacement at $x = \lambda/4$ by open circles. The time is normalized by the forcing period $T = 2\pi/\Omega$ and the surface displacement is normalized by the wavelength λ . The solid line shows the solution of Eq. (1), which was numerically integrated by the fourth-order Runge–Kutta method.

The results shown in Fig. 3 indicate that the calculation results agree satisfactorily with linear predictions. The small deviation comes from the evaluation error of the surface position in the

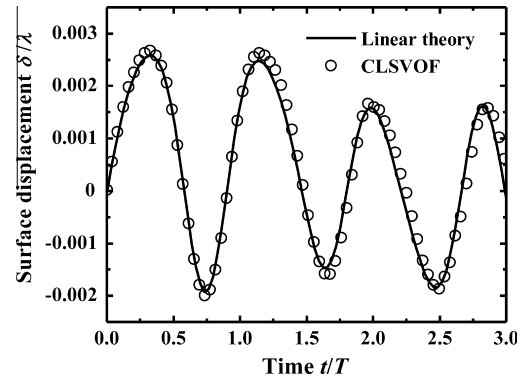


Fig. 3. Temporal evolution of the surface displacement at $x = \lambda/4$ obtained by the CLSVOF calculation (open circles) in comparison with the solution of Mathieu equation (solid curve) for the case $(X=1, Y=1.5)$ represented by the label “a” in Fig. 1.

CLSVOF method, in which the interface is implicitly defined as the null LS function $\phi = 0$ in a grid system of grid size $\lambda/64$. Further refinement of the grid size diminished the deviation.

3.2. Nonlinear regime

Our objective in this study is ligament formation, which is typically accompanied by large surface deformation. Thus, it is necessary to validate our approach for large surface deformation. Because we only considered one wavelength for each calculation, direct comparison with experimental results is difficult. We treated the case ($X = 0.88$, $Y = 0.25$) and $y_0 = \lambda$ denoted by label “b” in Fig. 1, which was also simulated by Wright et al. (2000) using the vortex-sheet method in two dimensions. The physical conditions were $\rho_l = 1000 \text{ kg m}^{-3}$, $\rho_g = 20 \text{ kg m}^{-3}$, $\sigma = 0.072 \text{ N m}^{-1}$, $\Omega = 6.28 \times 10^6 \text{ rad s}^{-1}$ ($f = 1 \text{ MHz}$), $\lambda = 12.19 \text{ }\mu\text{m}$, $\Delta_0 = 1.71 \text{ }\mu\text{m}$, and $\beta = 2.73$.

We compared our simulated results with those of Wright et al. (2000). Fig. 4(a) shows the temporal evolution of the surface displacement at $x = 3\lambda/4$, where the ligament eventually forms. The surface deformation response is sub-harmonic, and the overall tendency is the same in both calculations. The calculation results using the CLSVOF method are in quantitative agreement with the results of Wright et al. (2000) if the forcing phase is shifted as shown in Fig. 4(b) (their forcing phase being $3\pi/4$ more advanced than ours). The deviation observed near the end of calculation is due to the breakdown of the vortex-sheet simulation at the ligament disintegration stage (Wright et al., 2000).

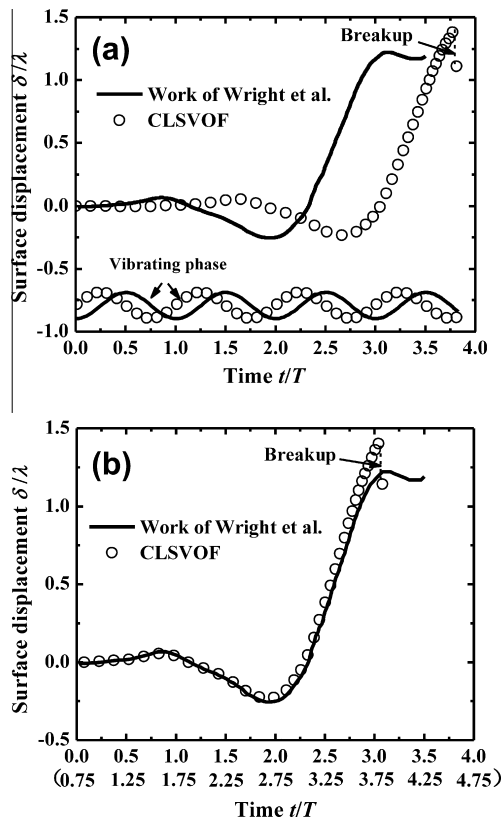


Fig. 4. Temporal evolution of the surface displacement at $x = 3\lambda/4$ obtained by the CLSVOF calculation (open circles) in comparison with the simulation results of Wright et al. (2000) (solid curve) for the case ($X = 0.88$, $Y = 0.25$) represented by the label “b” in Fig. 1. Panel (b) is the same comparison as (a) by shifting the forcing phase. The tick labels in the parenthesis denote the time in the CLSVOF calculation.

4. Dynamics of ligament formation

Although most of the past numerical calculations have focused on surface deformation, it is more important that the liquid-phase flow field is studied in detail to reveal the physical dynamics underlying ligament formation. Ultrasonic atomization experiments have shown that the frequency of the excited surface wave is equal to one half the forcing frequency (Lang, 1962; Donnelly et al., 2004). Therefore, we are especially interested in the typical ligament formation process appearing under sub-harmonic instability conditions in Fig. 1. As a prototype, we considered the case ($X = 0.9$, $Y = 0.3$) and $y_0 = \lambda$, corresponding to the real physical conditions given as follows: $\rho_l = 1000 \text{ kg m}^{-3}$, $\rho_g = 20 \text{ kg m}^{-3}$, $\sigma = 0.072 \text{ N m}^{-1}$, $\Omega = 1.27 \times 10^7 \text{ rad s}^{-1}$ ($f = 2 \text{ MHz}$), $\lambda = 7.20 \text{ }\mu\text{m}$, $\Delta_0 = 1.04 \text{ }\mu\text{m}$, and $\beta = 2.47$. This situation is close to the experimental observations made by Donnelly et al. (2004), in which the mean diameter of the produced aerosol for water was $2.61 \text{ }\mu\text{m}$ ($= (0.35 \pm 0.03)\lambda$) at $f = 1.95 \text{ MHz}$. The calculation conditions, including the case of harmonic instability and very large forcing amplitude, were also treated in the present study; we observed a common flow structure in the process of ligament formation. Therefore, the discussion on the detailed dynamics of ligament formation is based mainly on this prototype.

For convenience, we will refer to the “destabilizing phase” when the factor $(X \sin \hat{t} - Y)$ on the right-hand side of Eq. (1) is positive, because the destabilizing effect due to the positive inertial force overwhelms the stabilizing effect due to capillarity. The “stabilizing phase” will refer to the case where $(X \sin \hat{t} - Y) < 0$. For the prototype case with parameter pair ($X = 0.9$, $Y = 0.3$), the destabilizing phase refers to the period $(0.055 + n) < t < (0.445 + n)T$, where $n = 0, 1, 2, \dots$

4.1. Results of surface evolution

Fig. 5 shows the evolving liquid surface shapes and the liquid velocity vectors as viewed in the laboratory reference frame. The calculation starts at an instant when the bottom substrate moves upward from the middle position, and ends when the ligament disintegrates at its tip ($t = 3.65T$). During the initial stage until $t = 2.0T$, the surface deformation that is initiated by the small surface disturbance at $t = 0$ increases; however, its magnitude is small. Thus, the evolution of the surface deformation agrees well with linear theory, as can be seen in Fig. 6, which shows the temporal evolutions of the surface displacement at $x = 3\lambda/4$ obtained by linear theory and the CLSVOF calculation.

After $t = 2.0T$, the surface deformation becomes large, and the nonlinearity deviates the calculation result from the linear theory. The calculated increase in the surface displacement is abated and delayed compared with that provided by the linear predictions (Fig. 6). Moreover, according to linear theory, the direction of the surface deformation continues to alternate periodically with time, no matter how large the amplitude is. However, in the calculation, the ligament disintegrating into a droplet is formed. The broken droplet moves outward and never falls back because it holds a large outward vertical velocity in the laboratory reference frame, as shown for $t = 3.65T$ in Fig. 5. In the following sections, we will discuss the detailed dynamics that occur during the ligament forming process, in particular, the nonlinear effects associated with the slender freed ligament formation.

4.2. Destabilizing mechanism at the linear stage

The dynamics of the liquid layer during the destabilizing phase of the linear stage are easily understood qualitatively. Consider that the liquid layer has a simple step-like surface shape, as shown

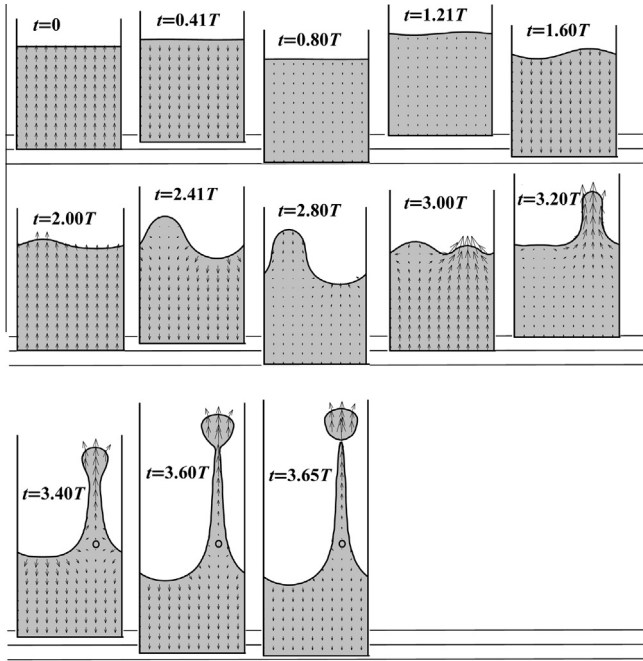


Fig. 5. Temporal evolution of the liquid surface shapes and the velocity vectors viewed in the laboratory reference frame for the case ($X = 0.9$, $Y = 0.3$) and $y_0 = \lambda$. The gray region represents the liquid while the white represents the gas. The velocity vectors are shown every six cells in both x - and y -direction for clarity. The three horizontal lines drawn in each row of figures denote the top limit position, middle position and bottom limit position of the vibrating substrate. The open circle shown after $t = 3.40T$ denotes the instantaneous stationary point where the velocity vanishes in the laboratory reference frame.

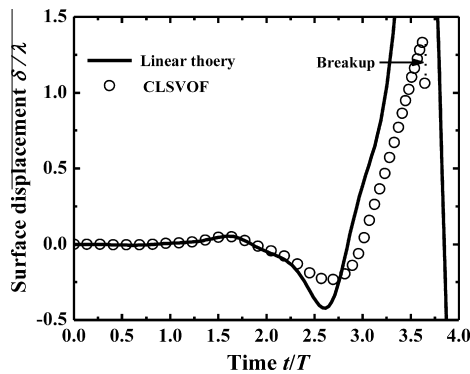


Fig. 6. Temporal evolution of the surface displacement at $x = 3\lambda/4$ obtained by the CLSVOF calculation (open circles) in comparison with the solution of Mathieu equation (solid curve) for the case ($X = 0.9$, $Y = 0.3$) and $y_0 = \lambda$.

in Fig. 7, in which the crest and trough portions are periodically repeated at wavelength intervals of $2\pi/k$ along the substrate. When the inertial force is directed upward (destabilizing phase), the pressure in the crest portion becomes lower than that in the trough portion at the same level. This pressure difference due to surface deformation exists only in the region near the surface. Thus, the region influenced by periodic surface deformation is, by phase mixing, restricted to a limited distance of $\sim 1/k$ from the surface. If the liquid layer is thick enough ($> 1/k$), then the pressure at the bottom should be uniform for the crest and trough portions ($p_R = p_L < 0$). The pressure difference near the surface induces liquid flow from the trough portion to the crest portion during every destabilizing phase. If this pressure difference is large enough to overcome the restoring capillary force, then the surface deformation will be enhanced, which strengthens the flow from the trough

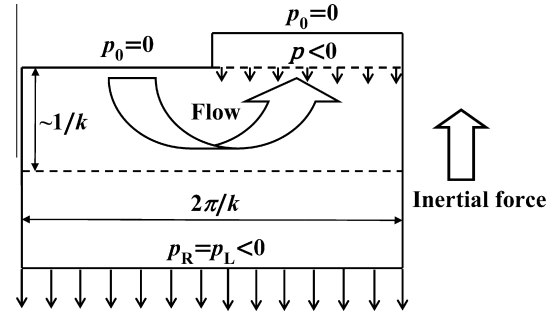


Fig. 7. A simple physical model for the linear instability mechanism of the Faraday wave. The surface shape changes periodically at an interval of $2\pi/k$ along the substrate. The arrows represent the pressure distribution.

to the crest. This is the mechanism of linear instability, which dominates in the initial stage when the surface deformation is small.

4.3. Ligament structure

For the purpose of the present study, we must well understand ligament formation from the surface resulting from nonlinear effects. This can be achieved by examining the dynamic structure of the largely deformed liquid layer in detail. Fig. 8 shows the pressure and vertical velocity distributions along the trough centerline and the crest centerline during the time span when the liquid surface becomes significantly deformed. Considering the flow structure difference, we divided the crest portion into three regions (I, II, and III), as shown in Fig. 9. In the following, we will discuss the dynamics of these three regions in detail.

4.3.1. Region I: Vicinity of the bottom substrate

For the thick layer case ($y_0 = \lambda > 1/k$), because the flow associated with the surface deformation is restricted within a limited distance from the surface, the magnitude of the velocity relative to the bottom substrate is small in Region I, and linear theory should be recovered. According to linear theory, the y -dependence of the vertical velocity follows $v(y) \propto \sinh(ky)$. Thus, between the bottom substrate and the surface, there exists a region where $v(y)$ obeys the exponential law $v(y) \propto \exp(ky)$ or $\lg[v(y)] \propto k \lg e \cdot y$ if the liquid layer is thick enough.

Fig. 10 shows the vertical velocity distribution at $t = 3.00T$, $t = 3.25T$, and $t = 3.50T$ at $x = 3\lambda/4$ where the centerline of the crest portion is located; these three time points all fall within the ligament forming process accompanying large surface deformation. The abscissa is plotted on a logarithmic scale. The straight line with slope $k \lg e$ is also drawn for reference. The numerical results in the region where the linearization assumption is valid agree well with the linear prediction. Additionally, the results indicated that even though the surface deformation is large, a layer of liquid where linear theory dominates still exists on the bottom substrate, as long as the liquid layer is thick enough. This layer has no significant effect on the dynamics of ligament formation. However, the thickness of Region I becomes thinner as time elapses because the nonlinear effects spread to the lower portion of the liquid layer as the trough surface moves downward.

4.3.2. Region II: Vicinity of the ligament root

In Region II, a local maximum pressure location forms (Fig. 9(b)), which is important for ligament formation. We first consider the thin-layer case ($y_0 = \lambda/4$), which is more convenient for investigating ligament formation dynamics. Later, an extended analysis to the thick-layer case ($y_0 = \lambda$) will be presented. In this study, the thin-layer case simply refers to a thickness of $y_0 = \lambda/4$,

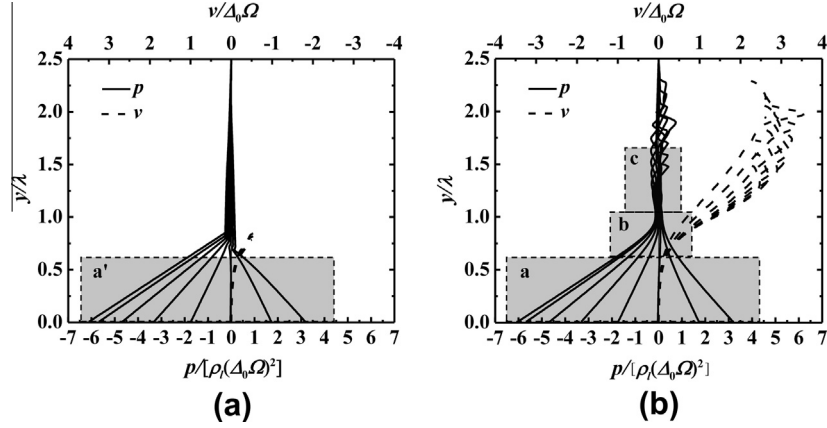


Fig. 8. Pressure and vertical velocity distributions along (a) the trough center line and (b) the crest center line during the time span from $t = 3.25T$ to $t = 3.60T$ when the liquid surface deforms largely. The enlargements of the pressure distributions enclosed by the dashed rectangles will be shown in Fig. 9.

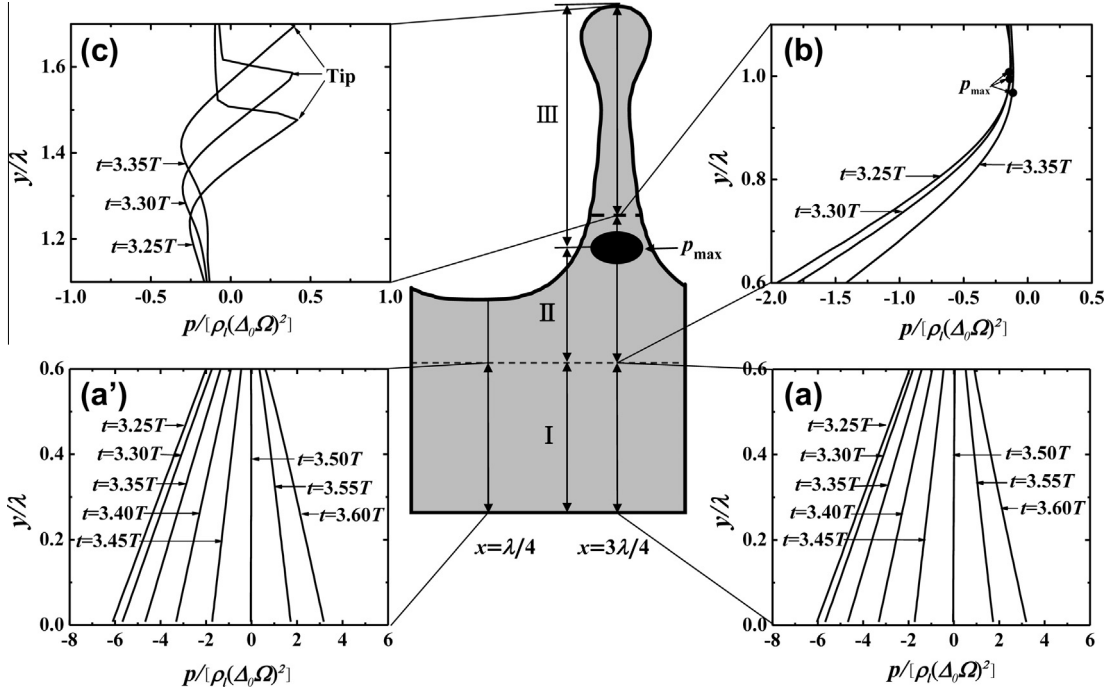


Fig. 9. Division of the ligament structure into Regions I, II and III and the enlargements of the pressure distributions in Fig. 8. Panels (a'), (a), (b) and (c) correspond to the dashed rectangles a', a, b and c in Fig. 8, respectively.

comparatively thinner than that used for the thick-layer case ($y_0 = \lambda$).

4.3.2.1. Thin-layer case. In the thin-layer case ($y_0 = \lambda/4$), the horizontal slip velocity allowable on the substrate surface may take a value comparable to the horizontal surface velocity component in magnitude, such that we can easily identify the two stagnation point locations B and C on the bottom substrate, as shown in Fig. 11. The temporal evolutions of these stagnation point locations are shown in Fig. 12, indicating that the location of the streamline trace ABCDE is fixed in space to a good degree.

In the vicinity of point C, the velocity can be evaluated as

$$u = -E(t) \cdot (x - 0.75\lambda), \quad v = E(t) \cdot y, \quad (12)$$

where $E(t)$ is the strain rate. Substituting Eq. (12) into the Euler equations around point C, we obtain

$$\rho_1 \left(\frac{dE}{dt} + E^2 \right) y = -\frac{\partial p}{\partial y} + \rho_1 g', \quad (13)$$

and

$$\rho_1 \left(-\frac{dE}{dt} + E^2 \right) (x - 0.75\lambda) = -\frac{\partial p}{\partial x}, \quad (14)$$

where $g' = \Delta_0 \Omega^2 \sin(\Omega t)$. Integrating Eq. (13) with respect to y from point C leads to

$$P(y, t) = p_c(t) + \rho_1 g' y - \frac{1}{2} \rho_1 \left(\frac{dE}{dt} + E^2 \right) y^2, \quad (15)$$

where $P(y, t)$ is the instantaneous pressure on the crest centerline and $p_c(t)$ is the pressure at the stagnation point C. Similarly, integrating Eq. (14) with respect to x leads to

$$p(x, y, t) = P(y, t) - \frac{1}{2} \rho_1 \left(E^2 - \frac{dE}{dt} \right) (x - 0.75\lambda)^2. \quad (16)$$

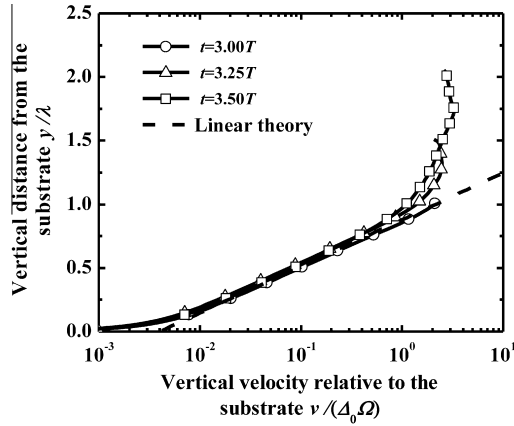


Fig. 10. Distribution of the vertical velocity relative to the bottom substrate along the crest center line ($x = 3\lambda/4$) at three instants. The velocity is relative to the bottom substrate. The dashed line represents the exponential distribution derived from linear theory.

Therefore, the pressure in the vicinity of point C is

$$p(x, y, t) = p_c(t) + \rho_1 g' y + \frac{1}{2} \rho_1 \frac{dE}{dt} [(x - 0.75\lambda)^2 - y^2] - \frac{1}{2} \rho_1 E^2 [(x - 0.75\lambda)^2 + y^2]. \quad (17)$$

From the third and fourth terms on the right-hand side of Eq. (17), we can distinguish two types of stagnation-point flows, as shown in Fig. 13. The streamlines of the two flow types are the same; however, the pressure distributions are totally different. The linear solution for which E^2 is a negligibly small value corresponds to the type-A stagnation-point flow only (depicted in Fig. 13(a) and referred to as a “linear stagnation-point flow”). The isobaric lines (obtained from the third term on the right-hand side of Eq. (17)) are hyperbolic curves. In the destabilizing phase, the decrease in pressure at the crest root (located above point C), whose magnitude is proportional to the crest height, sucks the surrounding liquid and increases the crest height. The increased crest height further lowers the crest root pressure. This is the mechanism behind the linear instability discussed in Section 4.2, which dominates at the early stages of crest development.

However, the nonlinear effect (i.e., the contribution of the convective terms in Eqs. (13) and (14)) is not negligible when the

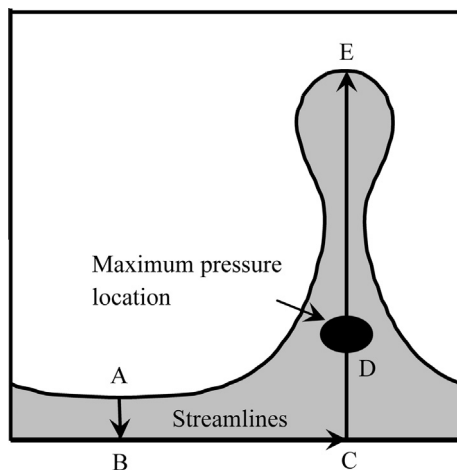


Fig. 11. Streamline passing through two stagnation points B and C in the thin layer case $y_0 = \lambda/4$. The location of streamline ABCDE is fixed in space as shown in Fig. 12.

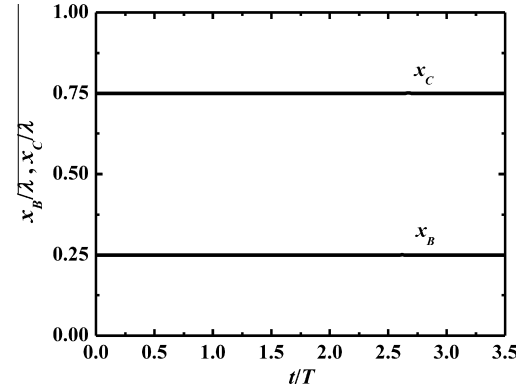


Fig. 12. Temporal evolutions of the left (B) and right (C) stagnation point locations for the thin layer case $y_0 = \lambda/4$.

magnitude of the flow velocity increases. Under these conditions, the type-B stagnation-point flow (depicted in Fig. 13(b) and referred to as a “nonlinear stagnation-point flow”) gradually becomes the dominant flow. As a result, the pressure at the crest root tends to increase and suppresses the suction effect, which changes the exponential crest-height increase over time in the linear regime to the almost linear crest-height increase with time in the nonlinear regime, as shown in Fig. 6. The ligament formation mechanism can be understood as pressure enhancement caused by the type-B stagnation-point flow as described below.

At $x = 0.75\lambda$, Eq. (17) can be written as

$$p(x, y, t)|_{x=0.75\lambda} = p_c(t) + \rho_1 g' y - \frac{1}{2} \rho_1 \left(E^2 + \frac{dE}{dt} \right) y^2. \quad (18)$$

Along the crest centerline, the pressure gradient $\partial p / \partial y$ is given by

$$\frac{\partial p(x, y, t)}{\partial y} \bigg|_{x=0.75\lambda} = \rho_1 g' - \rho_1 \left(E^2 + \frac{dE}{dt} \right) y. \quad (19)$$

Fig. 14 shows the temporal evolutions of dE/dt and E^2 during the destabilizing phase from $t = 3.055T$ to $t = 3.445T$. From Eq. (19), once both g' and $(E^2 + dE/dt)$ become positive, pressure maximizes at position y_D (corresponding to point D in Fig. 11). y_D is given by

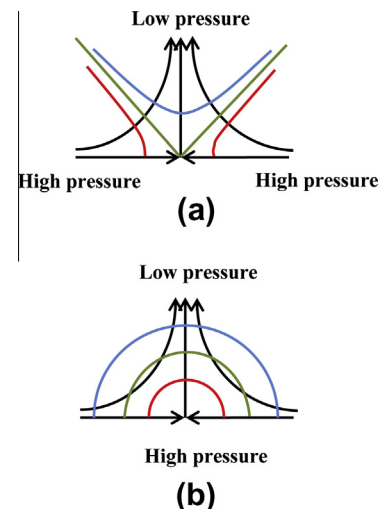


Fig. 13. Two types of stagnation-point flow around point C in Fig. 11: (a) linear stagnation-point flow and (b) nonlinear stagnation-point flow. The streamlines represented by arrowed lines are the same in both types, but the isobaric lines are hyperbolic curves for (a) and concentric circles for (b).

$$y_D = \frac{g'}{E^2 + \frac{dE}{dt}}. \quad (20)$$

In the early stages of the destabilizing phase, y_D calculated from Eq. (20) is larger than the crest height due to dE/dt and E^2 being small. Thus, this local maximum pressure location does not emerge in the early stages of the destabilizing phase. When y_D becomes smaller than the crest height, the maximized pressure location can be observed. Fig. 15 compares the value of y_D evaluated from Eq. (20) with that from the simulation results after the maximum pressure location emerges; the results are in good agreement.

The local maximum pressure location emerging at the crest root indicates that the pressure gradient vanishes there ($\partial p/\partial y = 0$). This means that the liquid between point D and the tip is dynamically free from the motion of the bottom substrate in the laboratory reference frame. In other words, the freed liquid region may have a chance of being released from the recovering motion of the liquid layer in the next stabilizing phase. The freed liquid region exhibits a totally different behavior from the amplified crest described by linear theory, in which no dynamically freed region from the substrate can be formed and the crest is always pulled back. As time elapses, the maximum pressure location moves downwards (see Fig. 15) and the new liquid elements passing through the maximum pressure location and entering the freed region will further enlarge the freed liquid region, resulting in a slender liquid ligament. This describes the essential feature of how the ligament is formed, and defines the necessary conditions for ligament formation as the emergence of the local maximum pressure location.

4.3.2.2. Thick-layer case. In the thick-layer case ($y_0 = \lambda$), the streamline coincident with the bottom substrate is not useful for characterizing Faraday wave flow because it is located outside of the region where the liquid flow is effectively associated with the surface deformation. However, similar arguments to those made for the thin-layer case can be used as follows.

Fig. 16 shows the velocity gradient $\partial v/\partial y$ and the pressure distributions along the crest centerline. The velocity gradient reaches a maximum at a location $y_V(t)$ around the crest root, where the pressure may be enhanced greatly due to the collision of liquids flowing from both sides. This pressure enhancement can be demonstrated in the following way. We set the numerical data attained at $t = 3.40T$ as the initial condition but the inertial force to zero. After one time step, we obtain the pressure distribution shown in Fig. 17, which excludes the effect of the inertial force and is entirely determined by the instantaneous liquid flow. It is apparent that the pressure enhancement at the crest root is caused by the impinging flow due to the convection terms.

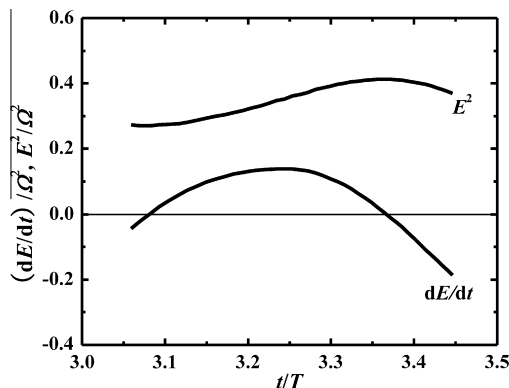


Fig. 14. Temporal evolutions of E^2 and dE/dt during the destabilizing phase from $t = 3.055T$ to $t = 3.445T$.

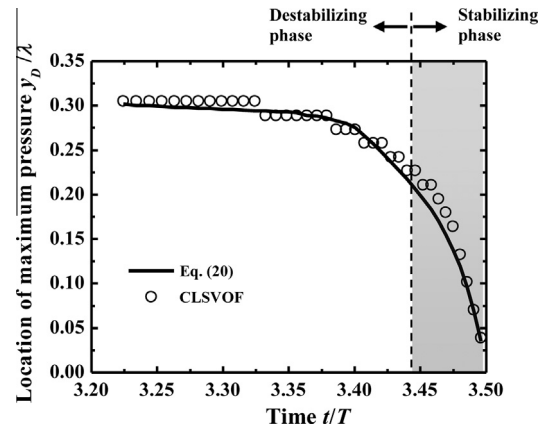


Fig. 15. Local maximum pressure location y_D evaluated from Eq. (20) in comparison with the simulation results in the thin layer case ($y_0 = \lambda/4$). The existence of the maximum pressure locations in the gray region indicates that the ligament keeps developing at the early stage of the next stabilizing phase.

From Fig. 16, the maximum pressure is always located around $y_V(t)$. Using the continuity equation, the horizontal velocity in the vicinity of $x = 0.75\lambda$ can be expressed as

$$u(x, y, t) = -\frac{\partial v}{\partial y} \Big|_{x=0.75\lambda} (x - 0.75\lambda). \quad (21)$$

Furthermore, in the vicinity of $y_V(t)$, where $\partial v/\partial y$ becomes maximized, the vertical velocity gradient and velocity are expressed as $E(t) = \partial v/\partial y|_{x=0.75\lambda, y=y_V(t)}$ and $v = v_Y + E(y - y_V)$, respectively, where $v_Y(t) = v|_{x=0.75\lambda, y=y_V(t)}$. Then, similar to the derivation of Eq. (17), we can derive an expression for the pressure in the vicinity of $y_V(t)$ as

$$p(x, y, t) = p_Y(t) + \rho_l(y - y_V) \left[g' - \left(\frac{dv_Y}{dt} - E \frac{dy_V}{dt} + E v_Y \right) \right] + \frac{1}{2} \rho_l \frac{dE}{dt} \left[(x - 0.75\lambda)^2 - (y - y_V)^2 \right] - \frac{1}{2} \rho_l E^2 \left[(x - 0.75\lambda)^2 + (y - y_V)^2 \right], \quad (22)$$

where $p_Y(t) = p|_{x=0.75\lambda, y=y_V(t)}$.

Eq. (22) is different from Eq. (17) due to the addition of the second term on the right-hand side of the equation. The location of maximum pressure is given by

$$y_D = \frac{g' - \left(\frac{dv_Y}{dt} - E \frac{dy_V}{dt} + E v_Y \right)}{E^2 + \frac{dE}{dt}} + y_V. \quad (23)$$

Considering that the free ligament is formed by the collision of liquids flowing at high speeds from both sides, the physics described here may apply to the splash formation problem treated by Josserand and Zaleski (2003), in which no such detailed considerations mentioning the delivery of a liquid sheet from the colliding liquid body have been provided.

4.3.3. Region III: Freed ligament region

The detailed development of the ligament region above the local maximum pressure location (Region III) can be more easily understood by expressing the vertical velocity distribution along the crest centerline, as viewed from the laboratory reference frame (v_a), for the thick-layer case ($y_0 = \lambda$) (Fig. 18). In this region, the abscissa y now stands for the distance measured from the position of the substrate before the start of the vibration. The instantaneous location of the local maximum pressure at the ligament root is indicated by a filled circle on each curve. Thus, a ligament dynamically freed from the substrate corresponds to the region

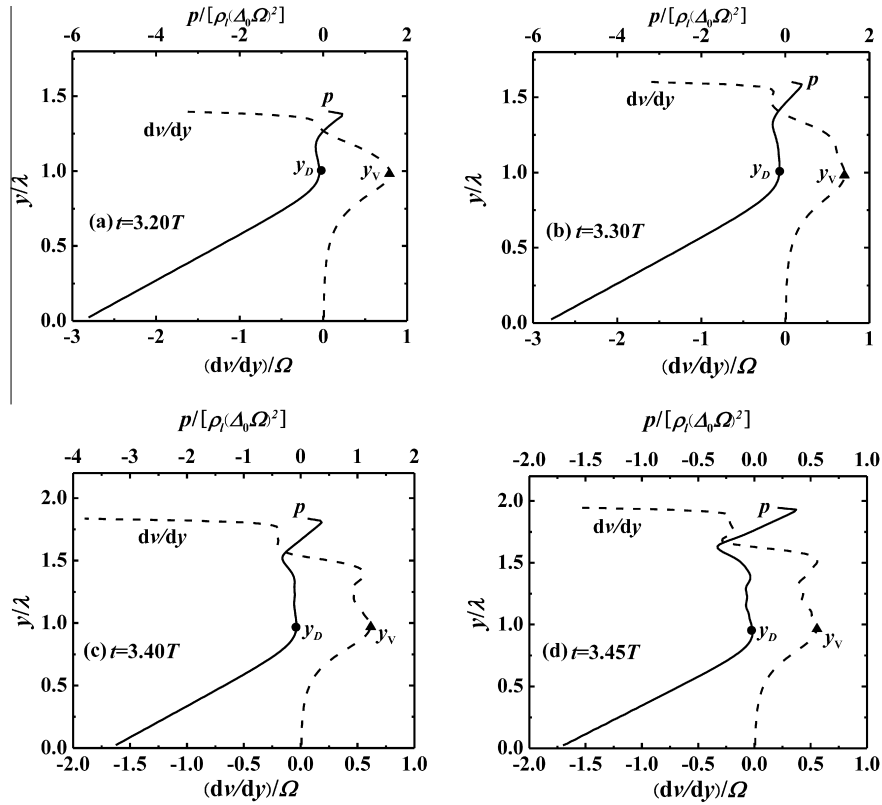


Fig. 16. Distributions of the velocity gradient $\partial v/\partial y$ (dashed lines) and pressure (solid lines) along the crest center line at (a) $t = 3.20T$, (b) $t = 3.30T$, (c) $t = 3.40T$, and (d) $t = 3.45T$. The maximum pressure location y_D is always near the maximum velocity gradient location y_V .

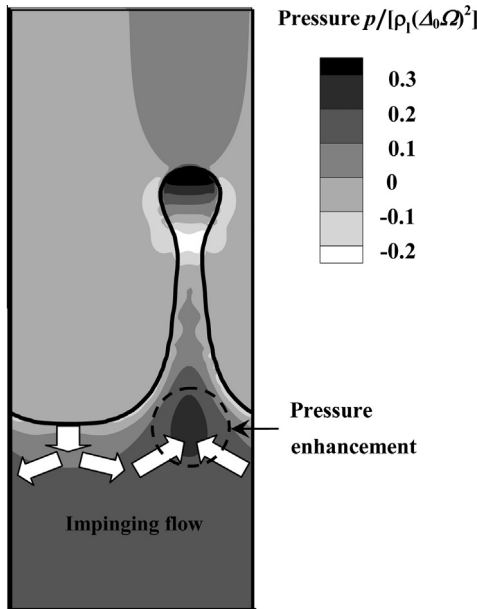


Fig. 17. Pressure distribution caused by an instantaneous flow. This figure is obtained by an artificial calculation to explain that the pressure enhancement at the crest root (dashed circle) is caused by the impinging flow (white arrows) from the neighboring trough portion.

to the right of the circle. The maximum pressure location emerges at $t = 3.20T$, and moves downward and disappears after $t = 3.50T$.

All of the ligament liquid elements above the maximum pressure location retain their vertical velocities in the laboratory reference frame. For example, the stationary point where $v_a = 0$,

indicated by the open circle in Fig. 5, keeps its position fixed after $t = 3.40T$ (see Figs. 5 and 18). This is because, for a freed ligament, whose ratio of thickness to length is small, the pressure relaxes to a uniform value consistent with the surrounding gas pressure ($\partial p/\partial y \cong 0$, see Fig. 9(c)), except for the ligament tip where the effect of contraction by surface tension is significant. Because an upper ligament element moves faster than a lower one, the upper element becomes thinner than the lower element with time. As a result, the freed ligament takes on a quasi-trapezoidal shape, narrowing upward. It is notable that the vertical velocity along the freed liquid region (except the tip portion) increases approximately linearly, as indicated by the dashed straight line in Fig. 18. The slope of the vertical velocity $\partial v/\partial y$ decreases with time. Standing at the location where the velocity vanishes, this ligament development process can be described by a simple model explained below.

Fig. 19 shows a schematic diagram of the ligament development model viewed in the laboratory reference frame, which can be recognized as an approximation of the liquid region above the stationary point $y = \xi$ (i.e. $y' = 0$ in Fig. 19), but excludes the ligament tip. The upper liquid mass moves upwards with a different vertical velocity along the vertical axis y , with no external force applied. The vertical velocity at the stationary point is zero, while the velocity at the top of this region is $v_t = dh(t)/dt = \text{const}$, where $h(t)$ is the height from the stationary point to the top. $h(t)$ can be expressed by $h(t) = h_0 + v_t t$, where h_0 is the initial height of the liquid mass. Because v_a gradually changes from 0 at $y' = 0$ to v_t at $y' = h(t)$, we assume that $\partial v_a/\partial y = v_t/h(t)$, consistent with the results shown in Fig. 18. Thus, the vertical velocity in the freed ligament portion is approximated by a straight broken line with a temporally decreasing slope. Applying the continuity equation to the whole region $0 < y' < h(t)$ leads to $db/dt = -bv_t/h$ and $da/dt = -av_t/h$, i.e., $b = b_0 h_0/(h_0 + v_t t) = b_0 h_0/h$ and $a = a_0 h_0/(h_0 + v_t t) = a_0 h_0/h$, which naturally conserves the area of the quasi-trapezoidal shape of the

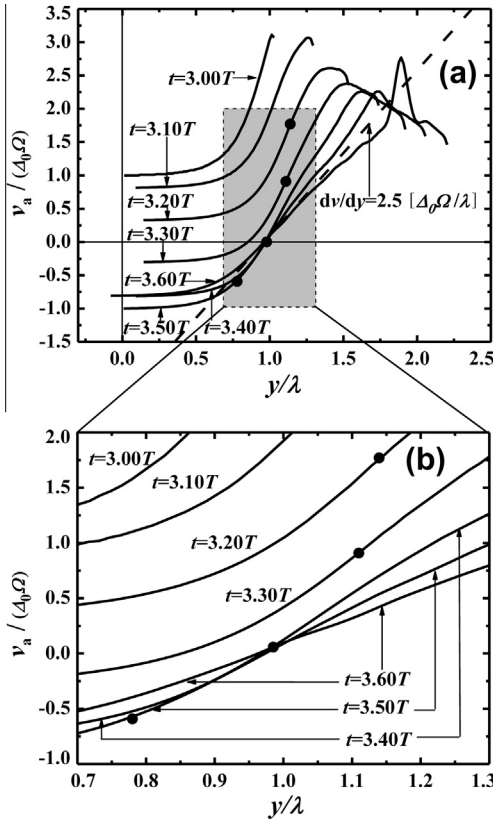


Fig. 18. Temporal change in vertical velocity distribution along the crest center line ($x = 3\lambda/4$) observed in the laboratory reference frame for the period from $t = 3.00T$ to $t = 3.60T$, during which ligament is formed. The abscissa y represents the distance from the initial location of the substrate surface. For clarity, the gray region in (a) is enlarged as shown in (b). The filled circle indicates the maximum pressure location at each instant, which moves down as time elapses and disappears after $t = 3.50T$. The vertical velocity in the freed ligament region can be approximated by a dashed straight line with a temporally decreasing slope.

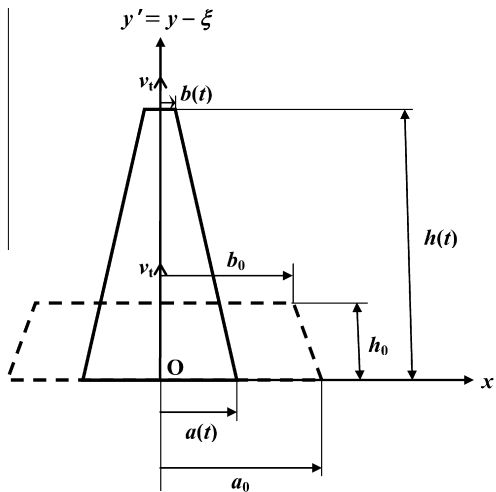


Fig. 19. A model of a freed ligament development. The initial shape is denoted as the dashed lines. The bottom corresponds to the stationary point ($v_a = 0$) as noted by the open circle in Fig. 5.

ligament: $(a + b)h = (a_0 + b_0)h_0$. The gradient of the ligament thickness distribution along the centerline is expressed by

$$\frac{b - a}{h} = \frac{(b_0 - a_0)h_0}{(h_0 + v_t t)^2}. \quad (24)$$

The gradient magnitude decreases with time. According to the assumption $b_0 < a_0$, this means that the left and right surfaces of the freed ligament tend to move toward the center, which results in a ligament of slender shape.

In the 3-D case, a significant difference appears in the ligament behavior due to the presence of circumferential surface tension. However, the freed ligament formed by an axis-symmetric flow about the ligament centerline has the same formation mechanism as the 2-D case. In particular, Eqs. (18)–(20) and (23) hold as they stand because the radially concentrating flow produced in the liquid layer only modifies the radial strain rate (equals to half the axial strain rate E). The dependence of the order of magnitude of the axial strain rate E on the forcing parameters is unchanged. Only the numerical value of the non-dimensionalized E will be modified. At the stage when the freed ligament develops, variation in the local ligament radius along the ligament is moderate. Therefore, the liquid passing the maximum pressure base tends to relax its pressure to a value determined by the local ligament radius r , i.e., $\sigma/r(y)$, instead of the surrounding gas pressure (zero). Correspondingly, the maximum pressure at the ligament base must be increased to a larger value. The breakup behavior of the freed liquid ligament is similar to that of an orifice liquid jet accelerated downward by gravity. Umemura et al. (2011) identified how the unstable waves responsible for breakups are produced in an accelerating water jet. In the present 2-D prototype calculations, the equivalent jet issue speed and acceleration rate are not large. In a similar jet issue condition, the 3-D ligament will disintegrate into droplets in a drip-like mode, for which the circumferential surface tension plays a secondary role, as captured in the present 2-D calculations. For the case when a long ligament forms, replacing the 2-D ligament width by the 3-D ligament cross-sectional area, Eq. (24) may be used to characterize a baseline ligament for the instability analysis of a 3-D ligament.

5. Conclusions

In this paper, we described how a liquid ligament connected to a liquid layer can be dynamically freed from the motion of the substrate. The flow associated with the periodic surface deformation is restricted to a finite thickness ($\sim 1/k$) of the near-surface liquid layer. When the surface deformation is small, its amplification is caused by the liquid flow from the trough portion to the crest portion due to the linear stagnation-point flow at the crest root formed during the destabilizing phase. Nonlinearity dominates gradually as the surface deformation increases. Correspondingly, the linear stagnation-point flow at the crest root is converted into a nonlinear stagnation-point flow. The pressure enhancement caused by the nonlinear stagnation-point flow brings about a local maximum pressure location at the root of the long ligament in which the pressure equilibrates with the surrounding uniform gas pressure. Therefore, the liquid ligament above the maximum pressure location is dynamically free from the bottom vibrating substrate in the laboratory reference frame. The liquid elements continuously pass through the maximum pressure location, which elongates the freed liquid region and results in a slender ligament.

References

- Al-Sueimani, Y., Collins, A., Yule, A., 1999. How orderly is ultrasonic atomization. In: Proc. of ILASS-Europe99.
- Al-Sueimani, Y., Yule, A.J., 2002. A CFD prediction of wave development and droplet production on surface under ultrasonic excitation. *Zaragoza* 9, 11.
- Benjamin, T.B., Ursell, F., 1954. The stability of the plane free surface of a liquid in vertical periodic motion. *Proc. Roy. Soc. Lond., Ser. A* 225, 505–515.
- Brackbill, J., Kothe, D.B., Zemach, C., 1992. A continuum method for modeling surface tension. *J. Comput. Phys.* 100, 335–354.

- Donnelly, T., Hogan, J., Mugler, A., Schommer, N., Schubmehl, M., Bernoff, A.J., Forrest, B., 2004. An experimental study of micron-scale droplet aerosols produced via ultrasonic atomization. *Phys. Fluids* 16, 2843–2851.
- Eggers, J., 1997. Nonlinear dynamics and breakup of free-surface flows. *Rev. Mod. Phys.* 69, 865–930.
- Eggers, J., Villermaux, E., 2008. Physics of liquid jets. *Rep. Prog. Phys.* 71, 036601.
- Faraday, M., 1831. On a peculiar class of acoustical figures; and on certain forms assumed by groups of particles upon vibrating elastic surfaces. *Philos. Trans. Roy. Soc. Lond.* 121, 299–340.
- Goodridge, C.L., Shi, W.T., Lathrop, D.P., 1996. Threshold dynamics of singular gravity-capillary waves. *Phys. Rev. Lett.* 76, 1824–1827.
- Goodridge, C.L., Shi, W.T., Hentschel, H., Lathrop, D.P., 1997. Viscous effects in droplet-ejecting capillary waves. *Phys. Rev. E* 56, 472–475.
- Goodridge, C., Hentschel, H., Lathrop, D., 1999. Breaking Faraday waves: critical slowing of droplet ejection rates. *Phys. Rev. Lett.* 82, 3062–3065.
- Harlow, F.H., Welch, J.E., 1965. Numerical calculation of time-dependent viscous incompressible flow of fluid with free surface. *Phys. Fluids* 8, 2182–2189.
- Hirt, C.W., Nichols, B.D., 1981. Volume of fluid (VOF) method for the dynamics of free boundaries. *J. Comput. Phys.* 39, 201–225.
- James, A., Vukasinovic, B., Smith, M.K., Glezer, A., 2003a. Vibration-induced drop atomization and bursting. *J. Fluid Mech.* 476, 1–28.
- James, A.J., Smith, M.K., Glezer, A., 2003b. Vibration-induced drop atomization and the numerical simulation of low-frequency single-droplet ejection. *J. Fluid Mech.* 476, 29–62.
- Josserand, C., Zaleski, S., 2003. Droplet splashing on a thin liquid film. *Phys. Fluids* 15, 1650–1657.
- Kumar, K., 1996. Linear theory of Faraday instability in viscous liquids. *Proc. Roy. Soc. Lond., Ser. A* 452, 1113–1126.
- Kumar, K., Tuckerman, L.S., 1994. Parametric instability of the interface between two fluids. *J. Fluid Mech.* 279, 49–68.
- Lang, R.J., 1962. Ultrasonic atomization of liquids. *J. Acoust. Soc. Am.* 34, 6–8.
- Miles, J., Henderson, D., 1990. Parametrically forced surface waves. *Annu. Rev. Fluid Mech.* 22, 143–165.
- Nichols, B., Hirt, C., Hotchkiss, R., 1980. SOLA-VOF: A Solution Algorithm for Transient Fluid Flow With Multiple Free Boundaries. Los Alamos Scientific Lab, NM, USA.
- Popinet, S., 2009. An accurate adaptive solver for surface-tension-driven interfacial flows. *J. Comput. Phys.* 228, 5838–5866.
- Qi, A., Yeo, L.Y., Friend, J.R., 2008. Interfacial destabilization and atomization driven by surface acoustic waves. *Phys. Fluids* 20, 074103.
- Rajan, R., Pandit, A., 2001. Correlations to predict droplet size in ultrasonic atomisation. *Ultrasonics* 39, 235–255.
- Renardy, Y., Renardy, M., 2002. PROST: a parabolic reconstruction of surface tension for the volume-of-fluid method. *J. Comput. Phys.* 183, 400–421.
- Rider, W.J., Kothe, D.B., 1998. Reconstructing volume tracking. *J. Comput. Phys.* 141, 112–152.
- Sethian, J., Smereka, P., 2003. Level set methods for fluid interfaces. *Annu. Rev. Fluid Mech.* 35, 341–372.
- Shinjo, J., Umemura, A., 2010. Simulation of liquid jet primary breakup: dynamics of ligament and droplet formation. *Int. J. Multiphase Flow* 36, 513–532.
- Sussman, M., 2003. A second order coupled level set and volume-of-fluid method for computing growth and collapse of vapor bubbles. *J. Comput. Phys.* 187, 110–136.
- Sussman, M., Fatemi, E., 1999. An efficient, interface-preserving level set redistancing algorithm and its application to interfacial incompressible fluid flow. *SIAM J. Sci. Comput.* 20, 1165–1191.
- Sussman, M., Puckett, E.G., 2000. A coupled level set and volume-of-fluid method for computing 3D and axisymmetric incompressible two-phase flows. *J. Comput. Phys.* 162, 301–337.
- Sussman, M., Smereka, P., Osher, S., 1994. A Level Set Approach for Computing Solutions to Incompressible Two-phase Flow. Department of Mathematics, University of California, Los Angeles.
- Takagi, K., Matsumoto, T., 2011. Numerical simulation of two-dimensional Faraday waves with phase-field modelling. *J. Fluid Mech.* 686, 409–425.
- Tan, M.K., Friend, J.R., Matar, O.K., Yeo, L.Y., 2010. Capillary wave motion excited by high frequency surface acoustic waves. *Phys. Fluids* 22, 112112.
- Tsai, S.C., Childs, P., Luu, P., 1996. Ultrasound-modulated two-fluid atomization of a water jet. *AIChE J.* 42, 3340–3350.
- Tsai, S.C., Luu, P., Childs, P., Teshome, A., Tsai, C.S., 1997. The role of capillary waves in two-fluid atomization. *Phys. Fluids* 9, 2909–2918.
- Umemura, A., 2011. Self-destabilizing mechanism of a laminar inviscid liquid jet issuing from a circular nozzle. *Phys. Rev. E* 83, 046307.
- Umemura, A., Kawanabe, S., Suzuki, S., Osaka, J., 2011. Two-valued breakup length of a water jet issuing from a finite-length nozzle under normal gravity. *Phys. Rev. E* 84, 036309.
- Van der Pijl, S., Segal, A., Vuik, C., Wesseling, P., 2005. A mass-conserving level-set method for modelling of multi-phase flows. *Int. J. Numer. Meth. Fluids* 47, 339–361.
- Vukasinovic, B., Smith, M.K., Glezer, A., 2004. Spray characterization during vibration-induced drop atomization. *Phys. Fluids* 16, 306–316.
- Vukasinovic, B., Smith, M.K., Glezer, A., 2007. Mechanisms of free-surface breakup in vibration-induced liquid atomization. *Phys. Fluids* 19, 012104.
- Wood, E., Loomis, A.L., 1927. XXXVIII. The physical and biological effects of high-frequency sound-waves of great intensity. *Lond., Edin., Dublin Philos. Mag. J. Sci.* 4, 417–436.
- Wright, J., Yon, S., Pozrikidis, C., 2000. Numerical studies of two-dimensional Faraday oscillations of inviscid fluids. *J. Fluid Mech.* 402, 1–32.
- Yule, A., Al-Suleimani, Y., 2000. On droplet formation from capillary waves on a vibrating surface. *Proc. Roy. Soc. Lond., Ser. A* 456, 1069–1085.